International Journal of Multiphase Flow 146 (2022) 103840

Contents lists available at ScienceDirect

International Journal of Multiphase Flow

journal homepage: www.elsevier.com/locate/ijmulflow

Phenomenology of bubble breakup and coalescence in sudden expansions and contractions in vertical pipes

C.M.P. Rosero [b], G.E.O. Celis [b], J.B.R. Loureiro [a,b,*], A.P. Silva Freire [a,b]

[a] Interdisciplinary Center for Fluid Dynamics (NIDF/UFRJ), R. Moniz Aragão 360, 21941-594, Rio de Janeiro, Brazil
[b] Mechanical Engineering Program (PEM/COPPE/UFRJ), C.P. 68503, 21941-972, Rio de Janeiro, Brazil

ARTICLE INFO

Keywords:
Multiphase flow
Bubble breakup
Bubble coalescence
Pipe expansion
Pipe contraction

ABSTRACT

The work discusses the phenomenology of bubble breakup and coalescence in a vertical pipe mounted with an expansion followed by a contraction. The flow conditions are such as to permit bubble-to-bubble-to-bubble, slug-to-bubble-to-slug and slug-to-slug-to-slug flow pattern transitions. Optical techniques are used to characterize the interactions between the phases (liquid–gas, gas–gas) and the resulting bubble breakup and coalescence processes. Thirteen sequences of events are used to illustrate the relevant processes. Breakup events are majorly ruled by the dynamic pressure forces of the turbulent motion. However, shear induced breakup is considerably observed for small and large bubbles. The formation of a gas pocket in the contraction is particularly identified as an important promoter of bubble breakup. Maps with the spatial location of bubble breakup for small and large bubbles and the changes in the velocities and lengths of Taylor bubbles as a result of their fragmentation and merging are also discussed for both singularities.

1. Introduction

A host of applications require the correct description of gas–liquid flows in pipes. Whereas it is very clear that in industry the predominant pipe lines keep a uniform cross section, one needs to bear in mind that complex piping systems can only be achieved with the help of multiple connecting parts, including enlargements and reductions.

In a recent contribution, Celis et al. (2021) used particle image velocimetry and the shadow sizer technique to investigate the dynamics of large and small bubbles in sudden expansions and contractions in vertical pipes. The experimental setup consisted of a 10.5-m vertical pipe mounted with an expansion at position $z = 3$ m (area ratio of 5.36) and a contraction at $z = 7$ m (area ratio of 0.19). The pipe diameters were 19 and 44 mm. The flow conditions were such that flow pattern transitions from bubble-to-bubble-to-bubble, slug-to-bubble-to-slug and slug-to-slug-to-slug were observed in the three characteristic stretches of the pipe (Fig. 1).

For small and long bubbles, the work introduced data on size and velocity distributions at six axial positions. For the continuous phase, results were presented for the mean velocity profiles, local shear rate and turbulent kinetic energy. The measured bubble velocity distributions were compared with predictions obtained through the classical theories of Davies and Taylor (1950), Nicklin et al. (1962), Zuber and Findley (1965), Wallis (1969) and Clift et al. (1978). The theory of Hinze (1955) was considered for an analysis of the largest permissible bubble diameter as a function of space coordinates and flow conditions. Hinze (1955) has clarified that the external forces controlling the splitting of a globule may be a viscous stress or a dynamic pressure set up in the surrounding continuous phase. The shear stress results from velocity gradients and the pressure difference from inertial effects (chaotic motion of the fluid).

The analysis identified a myriad of effects that ultimately resulted in bubble breakup and coalescence, including intense turbulent fields, interfacial instabilities, large regions of shear flow, secondary flows and streamline deflections. Most breakup events were ruled by turbulent agitation; however, shear induced breakup was also consistently observed for small and large bubbles. In the contraction, one particularly interesting noted phenomenon was the formation of a relatively steady gas pocket, which was observed to be an important promoter of bubble breakup.

The purpose of the present work is to offer a detailed account of the breakup and coalescence mechanisms briefly mentioned in Celis et al. (2021). The shadow sizer technique is used to describe the interaction of bubbles through sequences of single frames in a methodology that bears some resemblance to those of Galinat et al. (2005), Song et al. (2007) (both, optical techniques) and Keplinger et al. (2018) (X-ray). The work does not describe the interactions of a small number of bubbles created under idealized conditions, but rather complex configurations where a large number of bubbles freely interact with each

* Corresponding author at: Mechanical Engineering Program (PEM/COPPE/UFRJ), C.P. 68503, 21941-972, Rio de Janeiro, Brazil.
E-mail address: jbrloureiro@mecanica.coppe.ufrj.br (J.B.R. Loureiro).

https://doi.org/10.1016/j.ijmultiphaseflow.2021.103840
Received 12 December 2020; Received in revised form 16 April 2021; Accepted 23 September 2021
Available online 30 September 2021

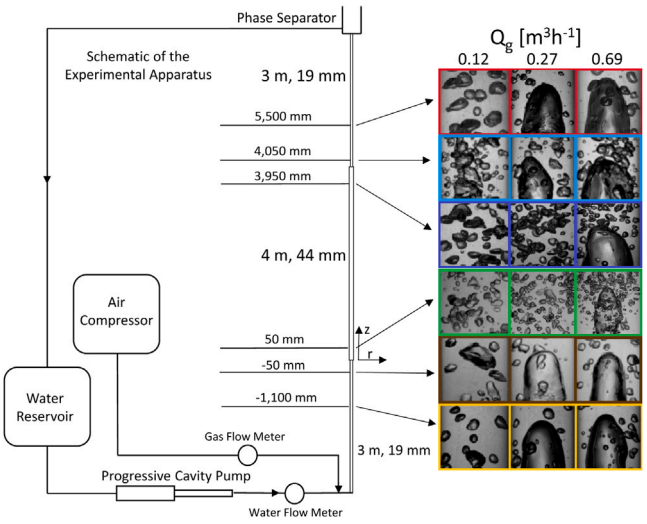

Fig. 1. Overview of the vertical pipe and the measurement positions. Q_l = 1.24 m^3h^{-1}; Q_g = 0.12, 0.27, 0.69 m^3h^{-1}. Location of the coordinate system.

other. Thus, every conceivable type of bubble breakup and coalescence was observed in the experiments.

In all, thirteen sequences of events are used to illustrate the coalescence and breakup processes that occur in pipe expansions and contractions. Sequences of bubble coalescence (*breakup*) followed by bubble breakup (*coalescence*) are well documented, revealing a very complex interaction process. Inasmuch as the contribution of Galinat et al. (2005), maps showing the location of bubble breakup are introduced for the large and small bubbles. These maps show that in the expansion the large bubbles break in a relatively limited region in the pipe centerline, whereas the small bubbles break over a very spread region that includes the near wall flow. In the contraction, the maps show a concentration of bubble breakup in the gas pocket fringes and in the central region of the pipe, right at the position of area reduction.

Changes in the velocities and lengths of the Taylor bubbles in the expansion and contraction regions as a result of their fragmentation and merging are also discussed. In the expansion, disturbances provoked by the shear layer that bounds the region of recirculating flow lead to multiple breakups and to a bubble translational velocity that is close to the values provided by the theory of Nicklin et al. (1962). In the contraction, the behavior of a Taylor bubble is shown to be more complex than that of a simple bubble stretching, as mentioned by Azzopardi et al. (2014), due to the breakup and coalescence of small bubbles in its tail. Here, a particular discussion on the observed changes in length, area and volume of long bubbles in a contraction is presented. We also show that the recorded Taylor bubble translational velocity downstream of a contraction is very close to the value predicted by the expression introduced in Nicklin et al. (1962).

2. Experiments

The experimental setup was abundantly discussed in Celis et al. (2021) and hence, for the sake of brevity, just the essential information is repeated here.

The basic experimental apparatus is shown in Fig. 1. The flow conditions are shown in Table 1. The working fluids are water and air.

The breakup and coalesce phenomena were characterized through a high speed shadow sizer system from Dantec Dynamics™. The basic elements of the system were two constellation led systems and a 12 bit Speed Sense M310 camera, with 1280 × 800 pixel resolution and maximum acquisition rate of 3260 frames per second. The camera was equipped with a 60 mm Micro Nikkor lens f/2.8D. The field of view ranged from 53.8(H) × 172.0(V) mm to 70.8(H) × 226.6(V) mm. The led systems had a controllable emission time (10 microseconds for the present measurements) and were triggered according to the acquisition frame rate adjusted for the camera (1400 frames per second for most of the experimental conditions). The camera was operated in single frame mode and the system synchronization was controlled by the software Dynamic Studio (version 2015a). The spatial resolution ranged between 5.65 to 10.55 pixel/mm, depending on the measurement station.

The image treatment followed the typical procedure introduced in Nogueira et al. (2003). As described in Celis et al. (2021), individual bubbles were processed by a dedicated contour detection algorithm implemented in MATLAB. A sequence of image processing operations, including subtraction of the mean background and correction of non-uniform brightness were applied to sharpen the contour of bubbles, so that edge detection could be accurately performed. Once a closed contour was determined, the position of the bubble centroid, i.e. the geometric center of the plane figure, given by the arithmetic mean position of all the points in the contour, was calculated.

The mean equivalent diameter (D_e) of a small bubble is defined as the diameter of a spherical particle having the same projected area as the area defined by the detected contour. For long bubbles, the length is defined as the distance between the top pixel on the bubble nose contour and the bottom pixel on the bubble tail. For bubbles bigger than the height of the field of view, the reconstruction method described in Matamoros et al. (2014) was applied.

The velocity of the bubbles was evaluated through a correlation similarity criterion to match a pair of bubbles. After the corresponding images of a same bubble in two consecutive frames were identified, the velocity was determined with sub-pixel accuracy.

The correct identification of overlapping bubbles is a renowned difficult task due to the different image intensity gradients resulting from in-focus and out-of-focus bubbles. Changes in bubble shape caused by turbulence and pressure differences also add a degree of complexity to the problem, particularly for moderate and small size bubbles. Despite the recent much attention devoted to the development of image processing algorithms Ferreira et al. (2012) and Fu and Liu (2016), many of the results available in literature are obtained through manual post-processing of high speed images. In the present work, the segmentation and the reconstruction of superposed small bubbles were individually processed through human intervention. Besagni and Inzoli (2016) used a similar procedure in the analysis of a bubble column. Considering the uncertainty of bubble diameter measurement through hand-picked points, Besagni and Inzoli (2016) showed that for small bubbles of equivalent diameter ranging from 1 to 9 mm the relative standard deviation varied between 12 to 2%, respectively.

The uncertainties of high-speed camera measurements depend on many parameters, including the frame rate, the exposure time, the illumination time and the magnification (Versluis, 2013). In the present experiments, these parameters were optimized to avoid blur and to furnish adequate spatial and temporal resolutions. Depending on the measurement station, the relative overall uncertainties with a confidence interval of 90% for the sizes and velocities of the small bubbles varied respectively from 1 to 11.5% and 5 to 12%. For long bubbles, the maximum relative overall uncertainties with a confidence interval of 90% for the lengths and velocities were of 0.5 and 1%, respectively. As mentioned by Besagni and Inzoli (2016), the larger the bubbles, the smaller the uncertainty measurements tend to be.

The extent of separated flow in the expansion and in the contraction, which are properties of the continuous field, were obtained through particle image velocimetry (PIV). For a full discussion on the PIV methodology, please, refer to Celis et al. (2021).

Table 1
Flow experimental conditions, where D_1 (= 19 mm) is the diameter of inlet and outlet segments, D_2 (= 44 mm) is the diameter of the intermediate segment, Q_l and Q_g are the volumetric liquid and gas flow rates in m^3h^{-1}, $U_{sl_{D_1}}$, $U_{sl_{D_2}}$, $U_{sg_{D_1}}$ and $U_{sg_{D_2}}$ are the superficial liquid and gas velocities at the inlet and intermediate segments, respectively.

Flow pattern ($D_1/D_2/D_1$)	Q_l (m^3h^{-1})	Q_g (m^3h^{-1})	$U_{sl_{D_1}}$ (ms^{-1})	$U_{sl_{D_2}}$ (ms^{-1})	$U_{sg_{D_1}}$ (ms^{-1})	$U_{sg_{D_2}}$ (ms^{-1})
Bubble/Bubble/Bubble	1.24	0.12	1.22	0.23	0.12	0.02
Slug/Bubble/Slug	1.24	0.27	1.22	0.23	0.26	0.05
Slug/Slug/Slug	1.24	0.69	1.22	0.23	0.68	0.13

3. The phenomenology of bubble breakup and coalescence

The qualitative description of the breakup and coalescence processes occurring in expansions and contractions introduced in this section is of great importance for the correct interpretation of the quantitative results of Celis et al. (2021). For a general description of bubble flow we recommend Wallis (1969) and Clift et al. (1978). Reviews on theories for the description of slug flow can be found in Gonçalves et al. (2018) and Fagundes Netto et al. (2019). The theoretical predictions for the behavior of long bubbles in slug flows to be shown next were obtained in accordance with the developments shown in Wallis (1969).

A few simple facts on the dynamics of small and large bubbles are introduced next.

3.1. Short comments on bubble dynamics

The theories reviewed in Wallis (1969) and Clift et al. (1978) for small bubbles introduce expressions for the rise velocity of confined and unconfined bubbles in terms of the Reynolds, Eötvös and Morton numbers. The Weber number is important to characterize bubble breakup and coalescence and is quoted here for completeness.

The relevant dimensionless groups can be cast as

$$R_e = \frac{\rho_l U_\infty D_b}{\mu_l}, \quad E_o = \frac{g(\Delta\rho)D_b^2}{\sigma}, \quad M_o = \frac{g\mu_l^4(\Delta\rho)}{\rho_l^2\sigma^3} \quad \text{and} \quad W_e = \frac{\rho_l U_\infty^2 D_b}{\sigma}, \tag{1}$$

where ρ_l = liquid density, μ_l = liquid viscosity, $\Delta\rho = \rho_l - \rho_g$, ρ_g = gas density, g = gravity acceleration, D_b = bubble diameter, σ = interface tension and U_∞ = terminal bubble velocity.

For small *fluid* spheres with $D_b < 1$ mm, the terminal velocity of an isolated bubble in a stagnant unconfined environment is given by (Wallis, 1969, *apud* Hadamard, 1911 and Rybczynski, 1911):

$$U_\infty = \frac{D_b^2 g(\rho_f - \rho_g)}{18\mu_f}\frac{3\mu_l + 3\mu_g}{2\mu_l + 3\mu_g}. \tag{2}$$

For large bubbles (20 mm < D_e), the effects of surface tension and viscosity are negligible. D_e denotes the bubble equivalent diameter, generally defined as the diameter of a spherical (*circular*) particle having the same volume (*area*) of a considered bubble. Large bubbles assume a spherical cap shape and their rise velocity is given by Wallis (1969) (*apud* Davies and Taylor, 1950):

$$U_\infty = (2/3)\sqrt{gR_c}, \tag{3}$$

where R_c is the radius of curvature in the region of the bubble's nose.

For bubbles of moderate size (1.3 mm < D_e < 20 mm), Clift et al. (1978) introduce

$$U_\infty = \left[(2.14\sigma/\rho_l D_e) + 0.505 g D_e\right]^{1/2}. \tag{4}$$

In a confined environment, the rise velocity of a bubble (U_b) is generally lower than that in unbounded liquids (U_∞). Corrections on the above expressions due to the influence of containing pipe walls, that is, of parameter D_e/D_p (where D_p denotes the pipe diameter) are introduced in Wallis (1969) (see also Celis et al., 2021).

In a flowing stream, the rise velocity of a single bubble or a train of bubbles traveling in a rectilinear path can be expressed as the sum of a term proportional to the mixture velocity and the weighted average drift velocity (Zuber and Findley, 1965), that is

$$U_{bf} = C_0 U_M + C_1 U_b, \tag{5}$$

where C_0 is the flow distribution parameter, related to the velocity and concentration profiles and U_M is the mixture velocity (=$(Q_g + Q_l)/A$, A = pipe cross section area). According to Wallis (1969), C_0 has a preferred value of 1.2 and $C_1 = 1$.

For isolate long bubbles of finite length in vertical tubes, U_{bf} is shown (Nicklin et al., 1962) to be well represented by

$$U_{bf} = 1.2U_M + 0.35\sqrt{gD_p}, \quad R_e > 8000. \tag{6}$$

In fact, as mentioned by Wallis (1969), in slug flows "the bubble drift velocity is not strictly constant since it is influenced by the velocity profile in the liquid slug". Hence, C_1 should be expressed in terms of the distance between bubble separation (l_s) and the pipe diameter. Only under conditions where l_s is large enough, slug flow can be considered relatively stable in terms of its structure so that Eq. (6) is valid. Here, we have used Eq. (6) to estimate the traveling velocity of long bubbles in vertical slug flow.

In terms of the volumetric flow rate, an approximate equation for the mean void fraction in slug flow is given by (Wallis, 1969),

$$\alpha = \frac{Q_g}{C_0(Q_l + Q_g) + C_1 A U_\infty}. \tag{7}$$

For long bubbles in vertical pipes, the weight of the liquid film surrounding the bubble is balanced by the wall shear stress resulting in a uniform thickness (δ) that can be obtained from falling film theory (see Wallis, 1969 for a description of the relevant equations). The held up liquid film decreases the length of the liquid slug and does not contribute to the pressure drop. For long bubbles, Wallis (1969) proposes a way of correcting Eq. (7) through

$$\alpha' = \alpha\left(1 - \frac{2\delta}{D_p}\right)^{-2}. \tag{8}$$

The length of the unit cell l_u can then be evaluated from $l_u = U_{bf}/\nu_t$, so that

$$l_f = \alpha' l_u, \tag{9}$$

where l_f denotes the length of the long bubble and ν_t is the frequency passage of bubbles, obtained from the experiments.

3.2. Flow in an expansion

3.2.1. Bubble-to-bubble flow pattern transition

The evolution of bubble flow in an expansion is illustrated in Fig. 2. To improve the visualization, the contours of the pipe wall and of some splitting and coalescing bubbles are also shown. The extent of the recirculating flow downstream of the expansion is marked by the *dashed* (*dotted*) lines. The mean and turbulent liquid velocity fields are discussed in Celis et al. (2021). The time evolution in Fig. 2 is uniform; the frames are shown (left to right) progressively in time, with a lapse of $10\Delta t$ (Δt = 1/1400 s).

Most bubble breakup and coalescence occurred due to turbulent effects. Collision provoked by the different rise velocity of bubbles, wake effects and turbulent agitation often result in bubble coalescence, in a process that is often followed by immediate bubble breakup (Fig. 2,

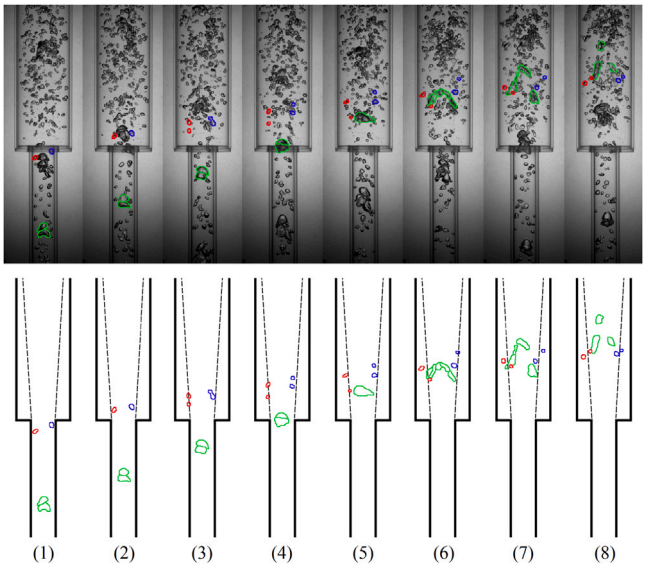

Fig. 2. Illustration of breakup and coalescence of small and moderate size bubbles in an expansion. The time interval between frames is $10\Delta t$, (Δt = 1/1400 s). Q_l = 1.24 m^3h^{-1}, Q_g = 0.12 m^3h^{-1}. The dashed lines indicate the extent of recirculating flow.

green contours). The breakup process is very complex and often a bubble is split into multiple parts. The net result of bubble interaction in the expansion is bubble breakup.

Bubble breakup due to shearing effects was also observed (Fig. 2, red and blue contours). Some of the small bubbles located near to the pipe wall enter the expansion and reach the high shear layer that bounds the recirculating flow region, illustrated through the dashed lines. The local velocity gradients elongate and rotate the initially spherical bubble to a dumbbell shape. The structure is continuously stretched until the connecting meniscus is disintegrated (Fig. 2, Frames 2–3). Most observed breakups due to shearing effects were binary, but some splittings resulted in three bubbles. The fragmented new bubbles are different in size and can eventually be captured by the separated flow region. In Fig. 2, Frames 6–8, small bubbles are trapped in the recirculation zone, attaining negative velocity values.

In addition to the central region of the pipe, small bubbles were observed to coalesce in the recirculating flow region, as shown in Fig. 3 (blue lines). Between Frames 2 and 4, three small bubbles coalesce resulting in a new bubble. Since in the recirculating flow region tracking the position of a bubble is a relatively easy task – due to the low concentrations, velocities and turbulence intensities – the characterization of breakup and coalescence events was very well determined. Observe that in Frames 8–12 the blue bubble hardly moves. Fig. 3 further illustrates bubble coalescence followed by very complex breakup (green lines). Two of the three bubbles shown in Frames 1–2 coalesce, resulting in a system of two bubbles that are further disintegrated into 5 (Frames 5–8) and 3 (Frames 8–9) small bubbles. The short time interval between frames (Δt = 1/1400 s) permitted a very good discrimination of bubble history, making it possible to distinguish "visual overlap" from significant events such as breakup and coalescence. Even very complex situations, with very dense clusters of bubbles, were well interpreted in view of the low Δt. Complex phenomena such as those shown in Fig. 3 were all analyzed frame-by-frame.

3.2.2. Slug-to-bubble flow pattern transition

For the intermediate gas flow rate (Q_g = 0.27 m^3h^{-1}), the turbulence levels in the expansion are already high enough to provoke the complete disintegration of the long incoming bubbles. The large Taylor bubbles are clearly discernible in the incoming 19-mm pipes; their nose, body and tail can be easily identified. Their relatively short length (33 mm on average, about $1.7D_1$) means that they are capable of entering the expansion without splitting but, as soon as they reach the midway length of the recirculation region, a catastrophic breakup event occurs in a very short time interval. From this point on, the long bubble completely loses its original form, the nose, body and tail cannot be identified anymore and are reduced to a swarm of small bubbles (Fig. 4). Much as for the previously discussed condition, coalescence and breakup were observed for the small bubbles, with a prevalence of the latter.

3.2.3. Slug-to-slug flow pattern transition

The general flow pattern and some aspects of the breakup of a long bubble (about $8D_1$ in length, D_1 = 19 mm) can be seen in Fig. 5. The disturbances on the large bubble contour are particularly shown.

The large bubble is observed to break at two instants of time, shown in Frames 6 and 8 (Fig. 5, from left to right). At Frames 4 and 5, the

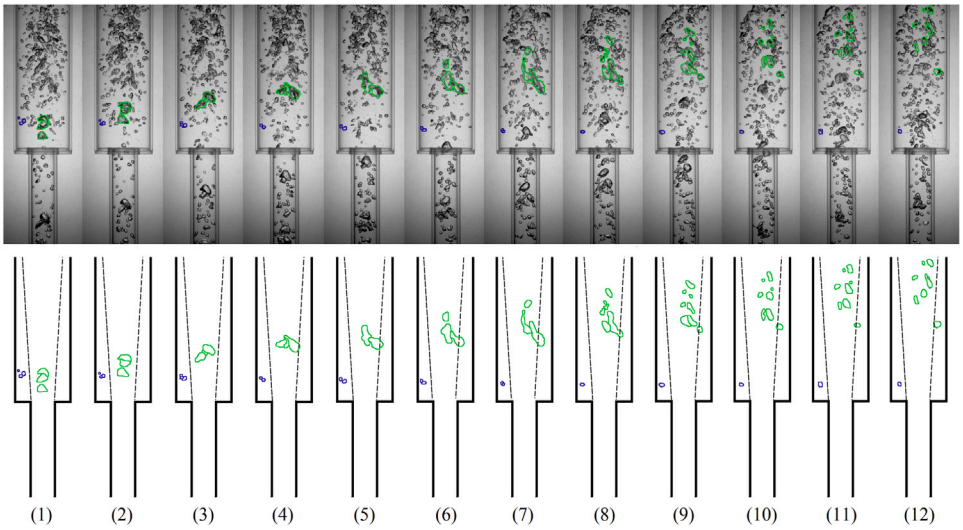

Fig. 3. Coalescence and breakup process of small and moderate size bubbles in an expansion. The time interval between frames is $10\Delta t$, (Δt = 1/1400 s). Q_l = 1.24 m^3h^{-1}, Q_g = 0.12 m^3h^{-1}. The dashed lines indicate the extent of recirculating flow.

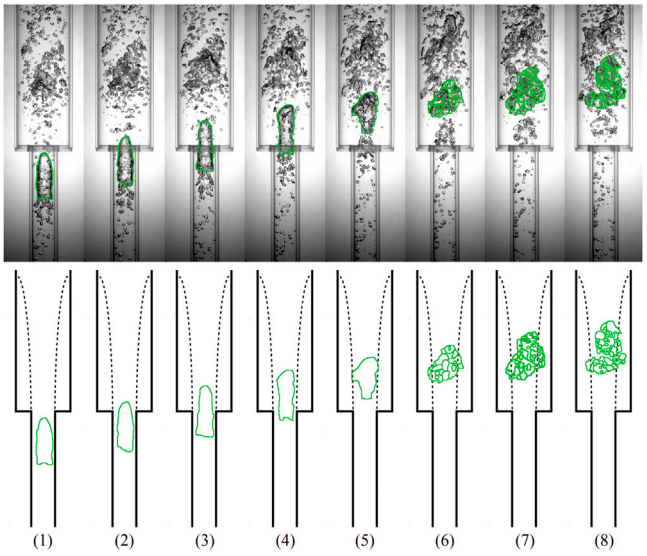

Fig. 4. Breakup of a large bubble entering the sudden expansion. The time interval between frames is $7\Delta t$, (Δt = 1/1400 s). Q_l = 1.24 m^3h^{-1}, Q_g = 0.27 m^3h^{-1}. The dashed lines indicate the extent of recirculating flow.

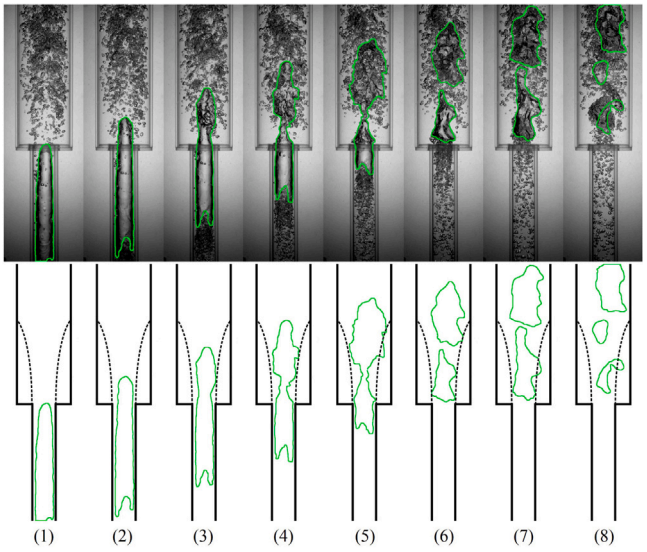

Fig. 5. Photographs of the time evolution of a large bubble entering the sudden expansion. The time interval between frames is $8\Delta t$, (Δt = 1/1400 s). Q_l = 1.24 m^3h^{-1}, Q_g = 0.69 m^3h^{-1}. The dashed lines indicate the extent of recirculating flow.

formation of a meniscus is clearly observed. The interface instabilities on the bubble starting at Frame 2 are amplified through Frames 3–6, where the rupture of the meniscus occurs and the first breakup is observed. The first breakup, thus, occurs in a time interval over 48 units of time (48/1400 s). The second breakup is ruled by the very high turbulence levels in the central region of the pipe and occurs in a much shorter time, under 8 time units. Despite the strong turbulent effects and the large deformation to which a long bubble is subjected, some of the surviving bubbles are still very large.

The behavior of a large bubble (about $3.75D_1$ in length) is shown in Fig. 6. The interface instabilities and the formation (and rupture) of a meniscus are also noted (Frames 2–5). The large translational velocity (U_{bf} = 2.18 ms^{-1}) and the limited length of the bubble do not prevent the occurrence of bubble breakup. The resulting small bubble, however,

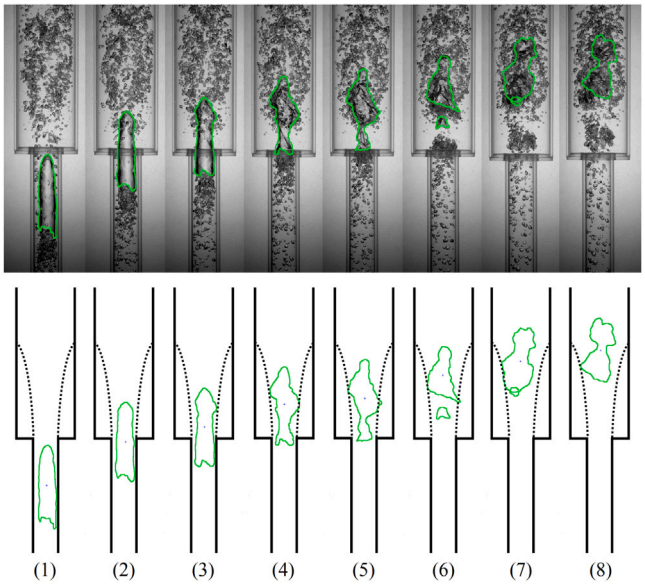

Fig. 6. Time evolution of a large bubble in an expansion. The time interval between frames is $2\Delta t$ (Δt = 1/1400 s). Q_l = 1.24 m^3h^{-1}, Q_g = 0.69 m^3h^{-1}. The dashed lines indicate the extent of recirculating flow.

immediately falls under the low pressure effects of the bubble wake (Frames 6–8) and merges back into the large bubble.

To further illustrate the above process, figures showing the lengths and the velocities of the bubbles can be constructed. In Fig. 7a, the abscissa z denotes the position along the height of the pipe where the nose of the bubble is located. The length of a long bubble, l_f, is defined as the distance between its fore and rearmost points. As a long bubble penetrates the expansion, the disturbances that lead to the meniscus formation and the bubble deformation provoke an initial increase in l_f, from 95 to 125 mm at positions −10 to 30 mm respectively. Between positions 30 and 94 mm, a stable bubble length is achieved with a relatively well defined plateau. Here, the term "stable length" denotes a bubble length that is not subjected to catastrophic changes due to breakup and coalescence.

At position z = 94 mm, the first breakup is observed. This event is marked by the discontinuity in the filled dot symbols and the appearance at position 34 mm of a second bubble (half filled dots) of length 58 mm. The first bubble experiences a sudden reduction in size, from 115 to 63 mm. The second bubble initially keeps a relatively stable length, which is followed by a sharp rise in size and a second breakup at z = 70 mm. The sharp increase in size is strongly influenced by the trailing wake of the first bubble (filled dots), in an effect that, however, is not strong enough to permit bubble reconnection as illustrated in Fig. 6. The prevailing effect, bubble breakup results from the very large levels of turbulence in the central pipe region, of about κ = 0.2 m^2s^{-2} (see Celis et al., 2021 for the complete distribution of κ in the expansion region). With the breakup, the size of the second bubble is reduced from 78 to 24 mm. The third bubble (empty dot symbols) appears at z = 40 mm, with a size of 28 mm.

The blue line shown in Fig. 7a illustrates the mean l_f (19 mm ID pipe) obtained from the vertical slug flow theory of Wallis (1969) (Eq. (9)). The red line shows the mean l_f obtained from the experiments.

The velocities of the nose, body and tail of a large bubble are shown in Fig. 7b. Since compressibility effects are absent, mass continuity implies that the mixture decelerates as a result of the increase in flow area. Indeed, as shown in Celis et al. (2021), the velocity of the continuous phase decreases continuously as the mixture flows through the expansion. The mean velocity of the nose of the bubble (red lines),

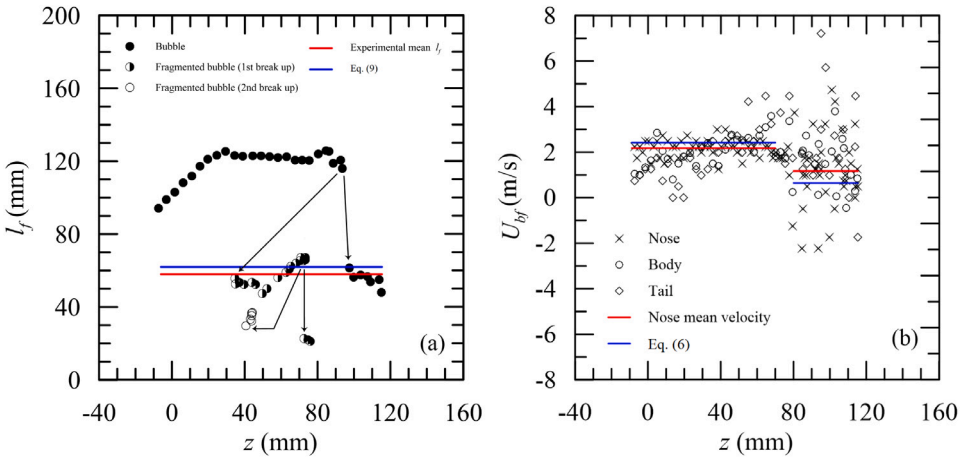

Fig. 7. Length and velocity of a Taylor bubble moving across a sudden expansion. The expansion is located at $z = 0$. In (a)–(b), z denotes the position of the bubble nose. The body velocity is the velocity of the centroid. Experimental flow rates, $Q_l = 1.24$ m^{3}h^{-1}, $Q_g = 0.69$ m^{3}h^{-1}.

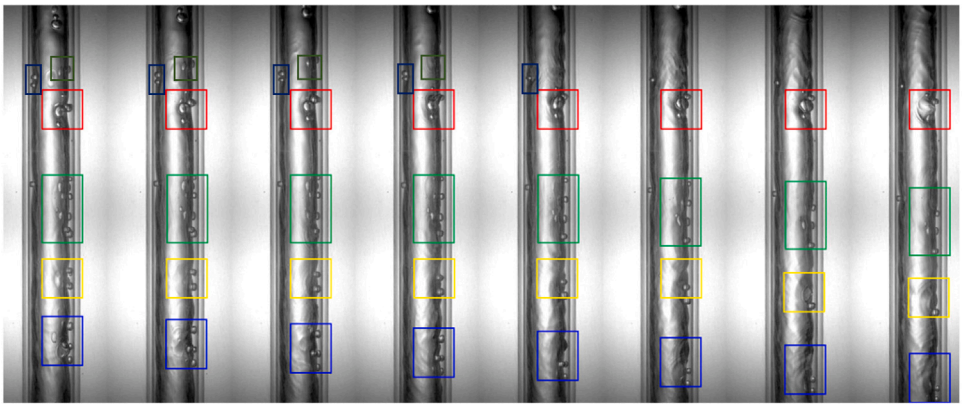

Fig. 8. Coalescence of small bubbles into a long bubble. $Q_l = 1.24$ m^{3}h^{-1}; $Q_g = 0.69$ m^{3}h^{-1}.

however, remains relatively constant (= 2.18 ms^{-1}) from position $z = -20$ to 60 mm, with a standard deviation (s) of 0.37 ms^{-1}. Downstream of position $z = 60$ mm, a decrease in U_{bf} is clearly noticed, despite the very large oscillations. From positions $z = 80$ to 120, the translational velocity of the bubble is 1.24 ms^{-1} with $s = 1.57$ ms^{-1}. The first bubble breakup occurs at about $z = 90$ mm, well into the region of very large velocity fluctuations.

For reference, the blue lines in Fig. 7b show the expected mean velocities for the long bubbles according to the theory of Nicklin et al. (1962). The top and bottom lines represent respectively the predicted velocities for the 19 and 44 mm pipes. In general, the measurements agree well with the predictions, but for the fact already mentioned that the velocities of the large bubbles just upstream of the expansion are observed to keep their magnitudes up to position $z \approx 60$ mm. This position is close to the position that marks the end of the region of recirculating flow (the reattachment point), $z = 73$ mm.

Bubble coalescence was observed in the recirculating flow region. Further coalescence occurred as a result of collisions induced by the distinct rise velocities of large and small bubbles. The coalescence of small bubbles onto the main body of a large bubble is a common occurrence in slug flow, as can be noticed in Fig. 8.

The presence of very long bubbles in the incoming pipe enhanced the coalescence of small bubbles into the long bubble as illustrated in Fig. 8. This coalescence mechanism is simple, has been observed before and is related to the thickness of the thin falling film that surrounds large vertical bubbles. Bubbles that are too big to be accommodated by the thin film are captured in the nose region of the large bubble. Bubbles of sizes comparable to the thickness of the film are squashed and coalesce onto the body of the long bubble. Previous studies on the dynamics of slug flow have observed and discussed the flux of gas in (*coalescence*) and out (*breakup*) of the long bubbles as a means to model the gas fraction of the liquid slug (see, e.g., Fernandes et al., 1983 and Andreussi and Bendiksen, 1989).

Most of the events observed in the expansion were breakup events.

3.2.4. Bubble breakup location in an expansion

Fig. 9 shows the location of small and large bubble breakups downstream of the expansion for one flow condition ($Q_l = 1.24$ m^{3}h^{-1}, $Q_g = 0.69$ m^{3}h^{-1}). The dashed lines represent the pipe walls and the dot-dashed lines illustrate the region of flow recirculation. The large bubbles break in the central area of the pipe with the rupture of the meniscus; most bubble splittings occur before the halfway length of the recirculating flow region is reached. The small bubbles break over a large region, in locations that span the entire pipe diameter. Fig. 9, however, suggests that the concentration of bubble breakups in the region immediately downstream of the expansion is very large, in the region of high turbulence, approximately 20 mm downstream of the expansion. No breakup event was observed in the recirculation region and in the central region of the expansion entrance. These observations agree with the results of Galinat et al. (2005), on an investigation of oil-in-water breakup downstream of an orifice plate.

3.3. Flow in a contraction

One typical and extremely important aspect of bubble breakup and coalescence at a contraction in vertical flows is the formation of a gas

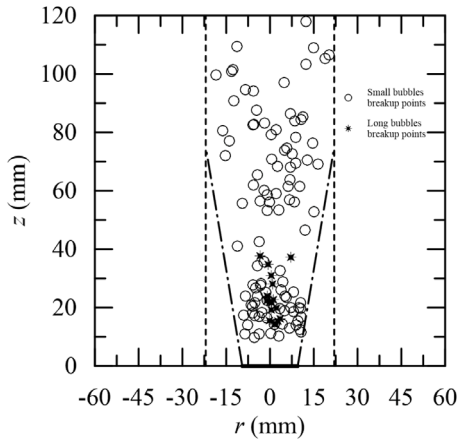

Fig. 9. Breakup location for small and large bubbles downstream of an expansion. Dashed lines represent the pipe walls and the dot-dashed lines illustrate the region of the recirculation region.

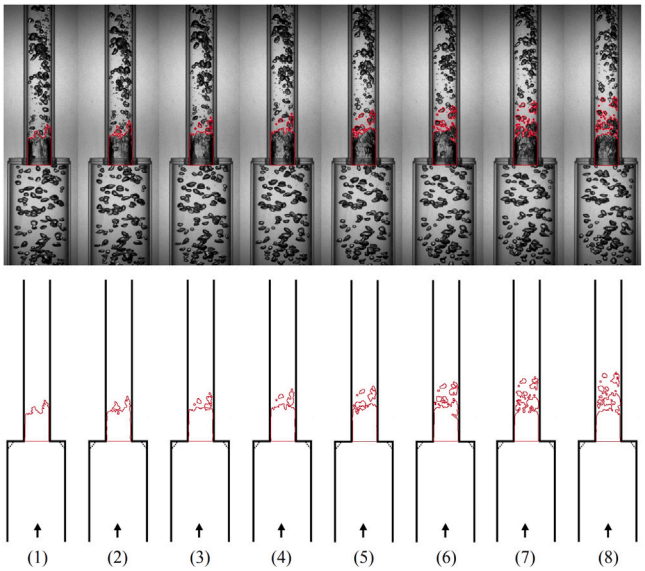

Fig. 10. Formation of a steady gas *vena contracta* during time intervals of $4\Delta t$, (Δt = 1/1400 s). Q_l = 1.24 m^3h^{-1}, Q_g = 0.12 m^3h^{-1}.

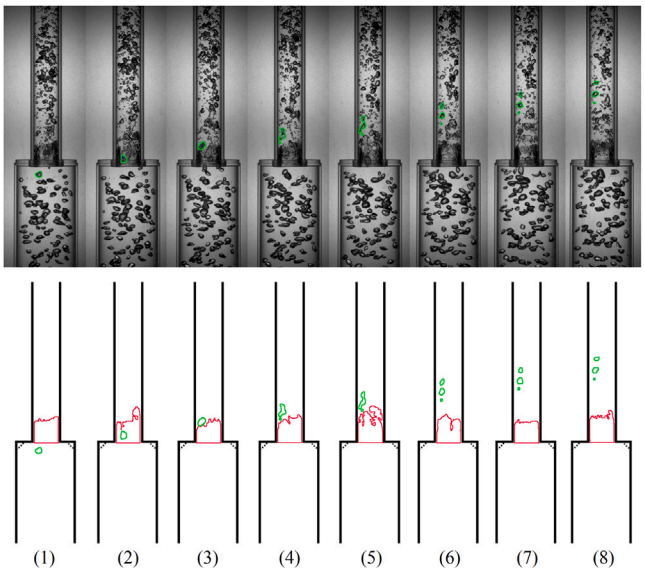

Fig. 11. Breakup process of small bubbles in a contraction: time evolution of bubbles during time intervals of $4\Delta t$, (Δt = 1/1400 s). Q_l = 1.24 m^3h^{-1}, Q_g = 0.12 m^3h^{-1}.

pocket. The gas pocket (or gas ring) is observed for both bubble and slug flows and plays the key role of forming a *vena contracta* with a complex unsteady behavior. In fact, depending on the incoming bubble conditions (size, spatial organization, velocities) the gas pocket can be stable or unstable. In the following, the conditions that lead to the formation and disintegration of the gas pocket are plenty discussed. As a simple rule, small bubbles coalescing at the entrance of the contraction form the gas pocket. Large bubbles capture and drag away the gas pocket, provoking its disintegration. The discussion below, however, reveals a much more complex picture with much more subtle aspects.

3.3.1. Bubble-to-bubble flow pattern transition

An incoming bubble flow normally creates the conditions for the establishment of a stable gas pocket. Small bubbles adhere and coalesce at the entrance of the contraction, forming a gas pocket that spans the complete perimeter of the pipe cross section (Fig. 10). The gas pocket is continuously fed by small bubbles until it reaches a certain stable configuration, resulting from a balance between the shearing-off of small bubbles from the pocket skirt and the arrival of new bubbles. The detachment of small bubbles from the gas pocket is a high frequency event that decisively contributes to the occurrence of a very large number of very small bubbles downstream of the contraction.

Another mechanism for small bubble breakup at the contraction is shown in Fig. 11. No fragmentation was observed near the upstream region of the contraction. However, upon entering the restriction, small bubbles are stretched by the flow that leaves the *vena contracta*, deform to a dumbbell shape and subsequently break. Fig. 11 shows a bubble that breaks into two parts.

3.3.2. Bubble-to-slug flow pattern transition

An increase in the gas flow rate leads to an increase in the number of bubbles that, under the effects of the converging flow at the contraction, tend to collide and coalesce (Fig. 12, Frame 1). As the resulting large bubble penetrates the 19-mm pipe, the gas pocket is strongly disrupted and dragged up (Frames 3–6) until it is completely absorbed by the large bubble (Frames 7–8). In Frame 7 the entrance of the contraction is free of a gas pocket, which is seen being reestablished in Frame 8. Many very small bubbles are noticed downstream of the contraction, as a result of their detachment from the gas pocket skirt.

The reestablishment of the gas pocket depends on the conditions of the flow resulting from the passage of a large bubble. In Fig. 13, the very large concentration of bubbles initiates the formation of a gas pocket. However, as further small bubbles coalesce at the entrance of the contraction, a moderate size bubble is formed at the pocket. With its growth in volume, the bubble detaches from the pocket, which is disintegrated. The large rising velocity of the detached bubble and its resulting turbulent wake induce further coalescence through collision and wake effects; these events promote a quick growth of the bubble (Fig. 13). After the short disruption, the gas pocket is reestablished and the process is repeated.

3.3.3. Slug-to-slug flow pattern transition

The passage of very large bubbles through a contraction has a strong effect on the gas pocket. Two possibilities would be expected to occur: the pocket (i) remains in its position or (ii) is displaced and merged with the long bubble as it passes through the contraction.

In the present work only case (ii) was observed (Figs. 14 and 15). In general, the large bubble is squeezed into the contraction through the gap generated by the gas pocket, resulting in a continuous elongation

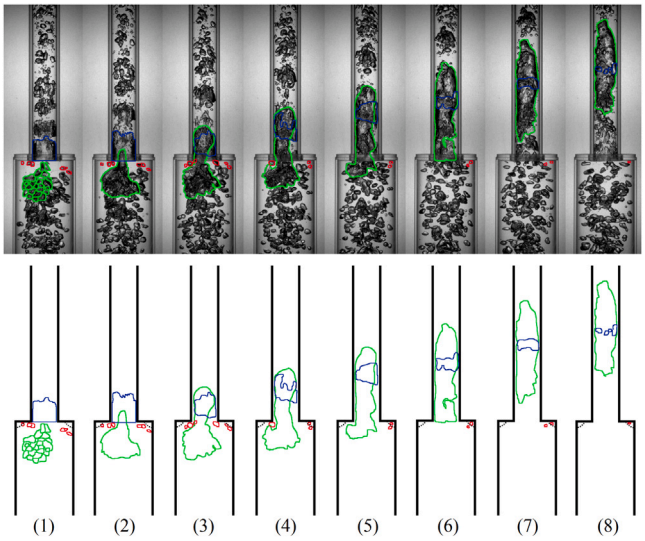

Fig. 12. Bubble coalescence at the contraction. Time intervals of $12\Delta t$, (Δt = 1/1400 s). Q_l = 1.24 m^3h^{-1}, Q_g = 0.27 m^3h^{-1}. The dotted lines indicate the extent of recirculating flow.

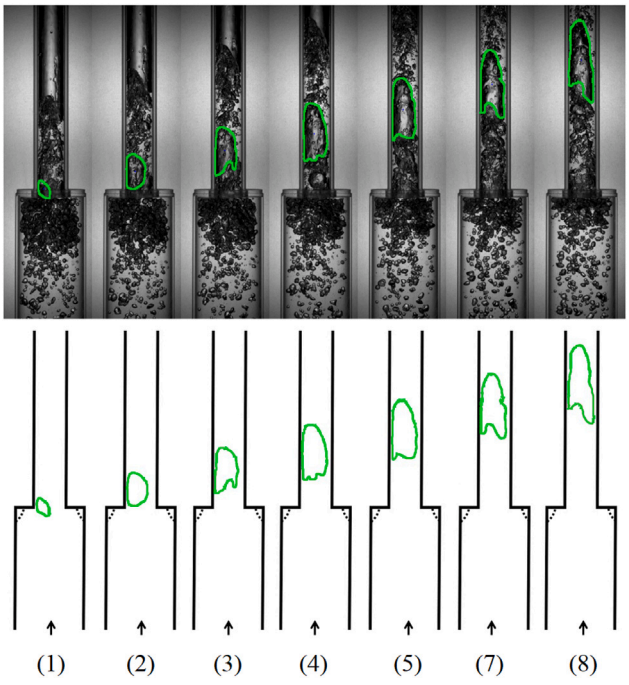

Fig. 13. Bubble detachment of the gas pocket. Time intervals of $12\Delta t$, (Δt = 1/1400 s). Q_l = 1.24 m^3h^{-1}, Q_g = 0.69 m^3h^{-1}. The dotted lines indicate the extent of recirculating flow.

that tends to preserve volume (Fig. 14). The complexity of the tail geometry, swarmed with small bubbles is clear. The position of the tail is defined by the rearmost point of the bubble.

The gas pocket region is illustrated in blue in Figs. 14 and 15, where two large bubbles of different sizes arrive at the contraction. The displacement of the gas pocket is apparent in both figures. The passage of a large bubble breaks and drags the gas pocket to a distance of about one or two diameters downstream of the contraction, when the pocket is finally consumed as the tail of the large bubble (and its low pressure wake) passes by. The deformation of the bubble tails in both figures is of interest to note.

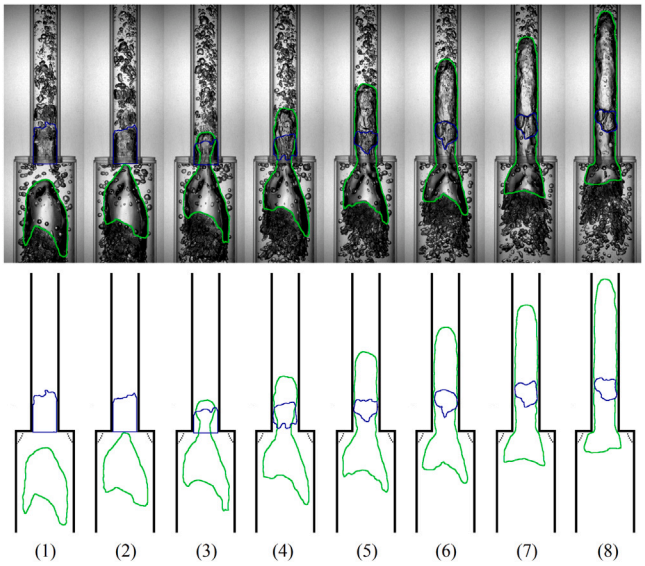

Fig. 14. Time evolution of moderate size bubble in a contraction. The time interval between frames is $12\Delta t$, (Δt = 1/1400 s). Q_l = 1.24 m^3h^{-1}, Q_g = 0.69 m^3h^{-1}. The dotted lines indicate the extent of recirculating flow.

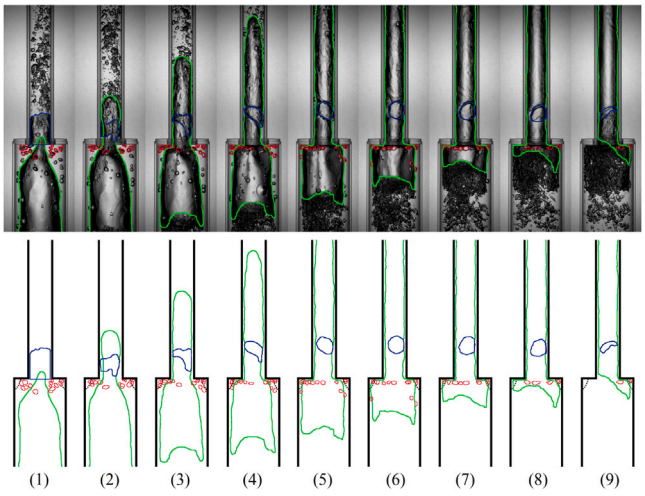

Fig. 15. Gas ring displacement by a large bubble. Time intervals of $25\Delta t$, (Δt = 1/1400 s). Q_l = 1.24 m^3h^{-1}, Q_g = 0.69 m^3h^{-1}.

Very long bubbles were observed to break at the contraction through the mechanism shown in Fig. 16. The bubbles are pushed into the contraction through the central region of the pipe where the momentum of the mixture is high. The result is the appearance of salient edges (Frames 2–4) that may not be capable of sustaining the required large distortions a bubble needs to undergo to penetrate the contraction. The following breakup originates a bubble that remains entrapped in the backward-facing step (Frame 5). This bubble subsequently enters the contraction (Frame 6) and rapidly grows in size as a result of small bubbles coalescence (Frame 7). The gas pocket of Frame 1 is displaced and incorporated by the bubble through Frames 2–4. Frame 5 shows no gas pocket, which begins to be reestablished in Frames 6–7.

The length and velocity of a large bubble moving across a contraction are shown in Fig. 17. At the contraction, the Taylor bubble is squeezed into the smaller pipe diameter, increasing its length almost continuously. According to Azzopardi et al. (2014), the increase in size follows from the stretching of the bubble as a result of volume

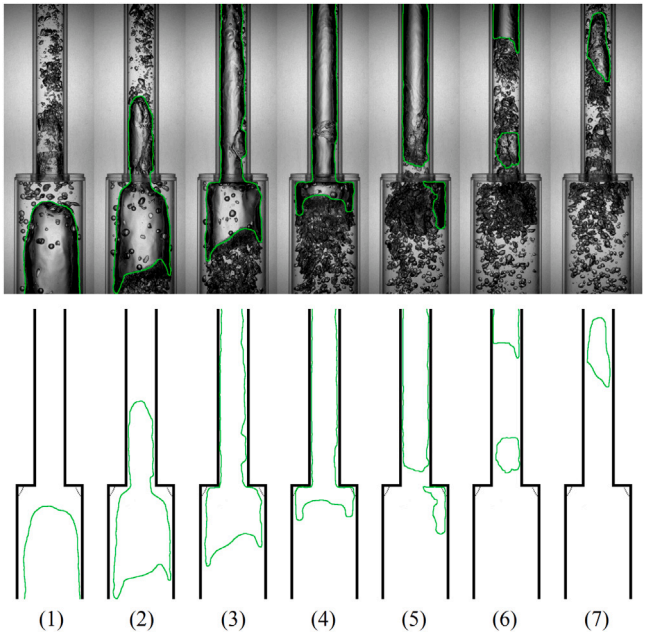

Fig. 16. Breakup of a large bubble in a contraction. Time intervals of $53\Delta t$, (Δt = 1/1400 s). Q_l = 1.24 m^3h^{-1}, Q_g = 0.69 m^3h^{-1}.

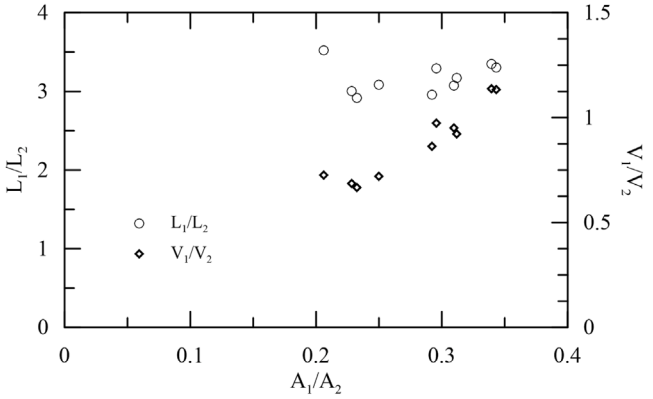

Fig. 18. Stretching of a long bubble in a contraction. A_1/A_2 = contraction ratio; L_1/L_2 = stretching ratio; V_1/V_2 = volume ratio.

conservation. Figs. 15 and 16 show that the process is, in fact, more complicate and that other effects are important for the definition of the bubble length. The coalescence of the gas pocket and the disruption of the bubble tail were already discussed. In addition, many small bubbles that are kept entrapped and almost at rest in the recirculating flow region behind the contraction coalesce into the large bubble as a result of collision (Fig. 15, Frames 2–4) and wake effects (Frames 7–9). The changes in length of the Taylor bubbles are shown in Fig. 18. The quantity A_1/A_2 in Fig. 18 corresponds to the ratio of the actual cross section area occupied by the bubbles in the pipes. On average, a reduction in area of 3.66 times is observed, which corresponds to changes in length and volume of 3.17 and 0.88 times respectively. The statistics on the volume of large bubbles is shown in Table 2.

The velocities of the nose, body and tail of a large bubble are shown in Fig. 17b. The clear steady increase in nose velocity from z = 3990 to 4000 mm results from the reduction in flow area due to the recirculation region. The velocity further increases due to the *vena contracta* (up to z = 4013 mm), relaxing downstream to U_{bf} = 2.38 ms^{-1} with s = 0.76 ms^{-1}. This value is particularly close to the value obtained through the theory of Nicklin et al. (1962) (= 2.42 ms^{-1}). Evaluating the tail and the body velocities was particularly difficult due to the observed large deformations. Fig. 17b, however, suggests that the velocity of the tail is considerably smaller than the velocity of the nose, as should be the case as the bubble is elongated. The body velocity is also suggested to have an intermediate value.

3.3.4. Bubble breakup location in a contraction

The places of small bubble breakup downstream of the contraction for Q_l = 1.24 m^3h^{-1} and Q_g = 0.69 m^3h^{-1} are shown in Fig. 19. The diamond symbols show the location of the bubble breakups originated in the gas pocket. This is a high frequency event that originates very small bubbles. The breakup positions of the bubbles arriving from the 44-mm pipe are marked by circles. The height of the gas pocket is about one pipe diameter (19 mm). Breakup events due to the high levels of turbulence are more frequent than shear induced breakup, which are, nonetheless, observed near the wall.

4. Final remarks

The present work complements the quantitative analysis of Celis et al. (2021) on the dynamics of small and large bubbles in expansions and contractions with a detailed description of the physical mechanisms that lead to the fragmentation and merging of bubbles.

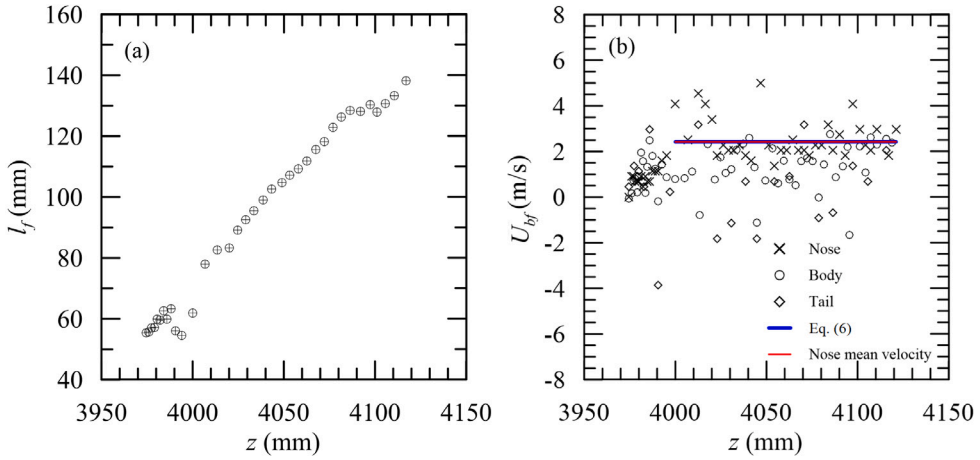

Fig. 17. Length and velocity of a Taylor bubble moving across a sudden contraction. The contraction is located at z = 4000 mm.

Table 2
Volume statistics of long bubbles (mm^3). Q_l = 1.24 m^3h^{-1}. s is the standard deviation.

	Q_g (m^3h^{-1})	0.27	0.69
z = −1,100 mm	V_{min}	1,719.11	3,822.82
	V_{max}	9,275.68	23,795.47
	V_{mean}	4,295.55	12,471.99
	s	1,182.93	3,203.81
z = −50 mm	V_{min}	2,000.26	2,882.84
	V_{max}	6,818.83	11,467.40
	V_{mean}	4,130.50	8,181.83
	s	1,002.60	1,736.48
z = 50 mm	V_{min}		7,041.54
	V_{max}		17,417.56
	V_{mean}		11,282.27
	s		2,862.72
z = 3,950 mm	V_{min}		24,473.76
	V_{max}		132,120.45
	V_{mean}		60,346.30
	s		34,172.96
z = 4,050 mm	V_{min}	5,493.77	4,279.93
	V_{max}	11,451.64	78,518.70
	V_{mean}	8,816.76	37,321.90
	s	2,168.51	22,504.13
z = 5,500 mm	V_{min}	2,222.01	25,178.84
	V_{max}	43,074.72	105,522.71
	V_{mean}	24,094.65	64,293.23
	s	8,864.01	17,377.26

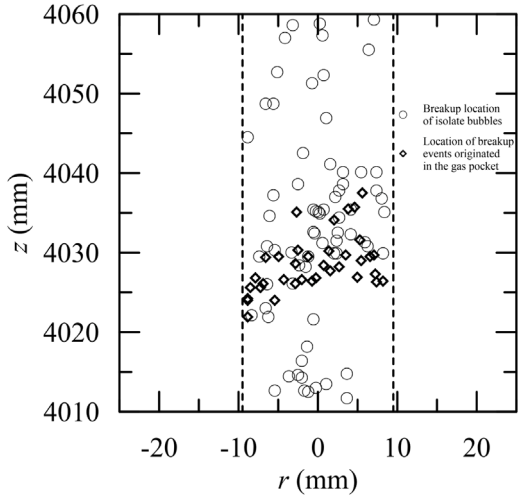

Fig. 19. Breakup location for small bubbles downstream of a contraction. The diamond symbols represent breakup events originated in the gas pocket. Isolate bubble breakup is represented by the circles.

The work shows that the dominant events in the expansions and contractions for small bubbles are breakups through turbulent dynamic pressure forces of the turbulent motions. Large bubbles in the expansion break due to disturbances provoked by the shear layer of the recirculating flow region and the high level of turbulence in the central region of the pipe. In the contraction, large bubbles are essentially stretched as they penetrate the smaller diameter pipe. Small bubbles may suffer significant velocity changes through expansions and contractions whereas long bubbles change considerably their velocities only in the contraction.

A large gas pocket formed at a contraction responds for much of the bubble breakup.

CRediT authorship contribution statement

C.M.P. Rosero: Investigation, Validation, Methodology, Data curation, Visualization. **G.E.O. Celis:** Investigation, Validation, Methodology, Formal analysis. **J.B.R. Loureiro:** Methodology, Writing – review & editing, Project administration, Resources. **A.P. Silva Freire:** Conceptualization, Validation, Writing – original draft, Supervision.

Declaration of competing interest

The authors declare that they have no known competing financial interests or personal relationships that could have appeared to influence the work reported in this paper.

Acknowledgments

APSF is grateful to the Brazilian National Research Council (CNPq) for the award of a Research Fellowship (No 307232/2019-0). JBRL is grateful for the financial support of FAPERJ E-26/203.257/2016 and CNPq 309455/2016-2. The work has been financially supported by FAPERJ, Brazil through grant E-26/010.001275/2016 (Pronex Núcleo de Excelência em Turbulência).

References

Andreussi, P., Bendiksen, K., 1989. An investigation of void fraction in liquid slugs for horizontal and inclined gas-liquid flow. Int. J. Multiph. Flow. 15, 937–946.
Azzopardi, B.J., Ijioma, A., Yang, S., Abdulkareem, L.A., Azzi, A., Abdulkadir, M., 2014. Persistence of frequency in gas-liquid flows across a change in pipe diameter or orientation. Int. J. Multiph. Flow. 67, 22–31.
Besagni, G., Inzoli, F., 2016. Bubble size distributions and shapes in annular gap bubble column. Exp. Thermal and Fluid Sci 74, 27–48.
Celis, G.E.O., Rosero, C.M.P., Loureiro, J.B.R., Silva Freire, A.P., 2021. Breakup and coalescence of large and small bubbles in sudden expansions and contractions in vertical pipes. Int. J. Multiph. Flow. 137, 103548.
Clift, R., Grace, J.R., Weber, M.E., 1978. Bubbles, Drops and Particles. Academic, New York.
Davies, R.M., Taylor, G.I., 1950. The mechanics of large bubbles rising through extended liquids and through liquids in tubes. Proc. R. Soc. London. Series A 200, 375–390.
Fagundes Netto, J.R., Gonçalves, G.F.N., Silva Freire, A.P., 2019. Statistical moments transport model for the prediction of slug flow properties. Int. J. Multiph. Flow. 120, 103086.
Fernandes, R.C., Semiat, R., Dukler, A.E., 1983. Hydrodynamic model for gas-liquid slug flow in vertical tubes. AIChE J 29, 981–989.
Ferreira, A., Pereira, G., Teixeira, J.A., Rocha, F., 2012. Statistical tool combined with image analysis to characterize hydrodynamics and mass transfer in a bubble column. Chem. Eng. J 180, 216–228.
Fu, Y., Liu, Y., 2016. Development of a robust image processing technique for bubbly flow measurement in a narrow rectangular channel. Int. J. Multiph. Flow 84, 217–288.
Galinat, S., Masbernat, O., Guiraud, P., Dalmazzone, C., Noik, C., 2005. Drop breakup in turbulent pipe flow downstream of a restriction. Chem. Eng. Sci. 60, 6511–6528.
Gonçalves, G.F.N., Baungartner, R., Loureiro, J.B.R., Silva Freire, A.P., 2018. Slug flow models: feasible domain and sensitivity to input distributions. J. Petroleum Sci. Eng 169, 705–724.
Hadamard, J.S., 1911. Mouvement permanent lent dune sphére liquide et visqueuse dans un liquide visqueux. Compt. Rend. Acad. Sci. Paris 152, 1735–1738.
Hinze, J.O., 1955. Fundamentals of the hydrodynamic mechanism of splitting in dispersion processes. A.I.Ch.E. J 3, 289–295.
Keplinger, O., Shevchenko, N., Eckert, S., 2018. Visualization of bubble coalescence in bubble chains rising in a liquid metal. Int. J. Multiph. Flow. 105, 159–169.
Matamoros, L.M.C., Loureiro, J.B.R., Silva Freire, A.P., 2014. Length-area-volume of long bubbles in horizontal slug flow. Int. J. Multiph. Flow. 65, 24–30.
Nicklin, D.J., Wilkes, J.O., Davidson, J.F., 1962. Two-phase flow in vertical tubes. Trans. Inst. Chem. Eng 40, 61–68.
Nogueira, S., Sousa, R.G., Pinto, A.M.F.R, Riethmuller, M.L., Campos, J.B.L.M, 2003. Simultaneous PIV and pulsed shadow technique in slug flow: a solution for optical problems. Exp. Fluids 35, 598–609.
Rybczynski, W., 1911. Über die fortschreitende Bewegung einer flüssigen Kugel in einem zähen Medium Bull. Acad. Sci. Cracovie A 4, 0–46.
Song, Y., Wang, D., Yin, J., Li, J., Cai, K., 2007. Experimental studies on bubble breakup mechanism in a Venturi bubble generator. Ann. Nucl. Energy 130, 259–270.
Versluis, M., 2013. High-speed imaging in fluids. Exp. Fluids 54, 1458–1493.
Wallis, G.B., 1969. One-Dimensional Two-Phase Flow. McGraw-Hill, New York.
Zuber, N., Findley, J.A., 1965. Average volumetric concentration in two-phase flow systems. J. Heat Transfer. Trans. ASME 87 (453).